

EBSD study of superplasticity: New insight into a well-known phenomenon

Mikhail Myshlyaev^{1,2}, Sergey Mironov^{3*}, Galia Korznikova⁴, Tatyana Konkova^{4,5}, Elena Korznikova⁴, Ainur Aletdinov⁴, Gulnara Khalikova⁴, George Raab⁶, Sheldon Lee Semiatin⁷

¹ Baikov Institute of Metallurgy and Materials Science, Russian Academy of Science, 49 Lenin Avenue, Moscow 119991, Russia

² Institute of Solid State Physics, Russian Academy of Sciences, 2 Academic Osypian Street, Chernogolovka 142432, Russia

³ Belgorod National Research University, 85 Pobeda, Belgorod 308015, Russia

⁴ Institute for Metals Superplasticity Problems, Russian Academy of Science, 39 Khalturin Street, Ufa 450001, Russia

⁵ University of Strathclyde, 75 Montrose Street, Glasgow G1 1XJ, United Kingdom

⁶ Ufa State Aviation Technical University, 12 K. Marx Street, Ufa 450008, Russia

⁷ Air Force Research Laboratory, Materials and Manufacturing Directorate, AFRL/RXCM, Wright-Patterson AFB, OH 45433-7817, USA

Electron backscatter diffraction (EBSD) was applied to investigate the superplastic behavior of a fine-grain Al-Mg-Li alloy. It was found that microstructural changes were noticeably influenced by the occurrence of continuous dynamic recrystallization. This mechanism involved a transverse subdivision of pre-elongated grains which eventually transformed into chains of nearly-equiaxed grains. A body of experimental observations, including extensive strain hardening, marked grain elongation, the formation of pronounced substructure in interior regions of grains, and the development of crystallographic texture, provided strong evidence of large amounts of intragranular slip operating during superplastic flow.

Keywords: Superplasticity; Metals and alloys; Electron backscatter diffraction (EBSD); Microstructure

*Corresponding author; email address: mironov@bsu.edu.ru

1. Introduction

It has been well accepted for a long time that the fundamental prerequisite for superplastic deformation is a relatively-fine equiaxed grain structure with a high fraction of high-angle boundaries. It is believed that such a microstructure is best suited for grain-boundary sliding which is usually recognized as the key mechanism of superplasticity. However, it has been conclusively demonstrated recently that materials with “non-ideal” microstructures may also exhibit superplasticity. Specifically, superplastic behavior has been found in materials with partially-recrystallized microstructures which contain a large fraction of low-angle boundaries [1-28], in very coarse-grain (~100 μm scale) materials [17, 29-39], and in lamellar-type microstructures [40-42]. In all such cases, the initial stage of superplastic deformation was characterized by the extensive occurrence of dynamic recrystallization which converted the “non-ideal” initial microstructure into the typical fine-grain one. As a general rule, this stage was also characterized by measurable strain hardening (with following strain softening), and subsequent steady-state flow was typically attributed to the activation of the grain-boundary sliding [2-9, 11, 12, 14, 15, 20-22, 25, 28, 35, 39-42]. A somewhat similar behavior has also been observed during superplasticity of bimodal grain structures [28, 43, 44]. In such instances, the coarse-grained constituent typically experiences continuous recrystallization whereas the fine-grained one undergoes grain-boundary sliding.

Clear signs of extensive intragranular slip have also been found in superplastically-strained materials with “ideal” fine-grain, well-recrystallized microstructures [10, 45-57]. Specifically, pronounced continuous recrystallization has been observed in various structural materials including aluminum alloys [10, 46, 47, 50, 54, 55, 57], titanium alloys [48, 49, 51, 53], magnesium alloys [52, 56], and duplex stainless steel [45]. In two-phase materials, this effect is sometimes attributed to strain partitioning between the softer and harder phases [58].

Taken together, the above observations suggest that a significant role is played by intragranular slip under superplastic-deformation conditions. In fact, these recent findings are in line with “old” theories (proposed in the 1960s-1990s) which suggested a close relationship between superplasticity and dynamic recrystallization [59-62].

The relatively-recent advent of high-resolution/high-speed electron backscatter diffraction (EBSD) [63] may provide new insight into intragranular slip activity occurring during superplastic deformation and thus the overall phenomenon itself. To date, however, investigations utilizing EBSD have been relatively limited. Therefore, the present EBSD effort was undertaken to quantify microstructural changes occurring during superplastic deformation of an “ideal” fine-grain[†] recrystallized material. The main emphasis was in-depth microstructural analysis which involved examination of grain size and morphology, the substructure within grains, misorientation distributions, crystallographic texture, and the orientation relationship between neighboring grains.

2. Materials and Procedures

The material used in the present work was the commercially-produced aluminum alloy 1420 (per the Russian designation) with a nominal chemical composition (in weight percent) of Al-5.5Mg-2.2Li-0.12Zr. This is a relatively simple alloy whose superplastic behavior has been well studied. Hence, it was considered to be particularly suitable for the purpose of the present effort. The material was received as hot-rolled plate with a fully-recrystallized microstructure and a mean grain size of 20 μm .

To produce a fine-grain microstructure appropriate for superplastic testing, the received alloy was solution treated at 470°C for 1 h, water quenched, and then subjected to 10 passes of equal-channel angular pressing (ECAP). ECAP was conducted at 370°C ($\approx 0.69T_m$, where T_m is the melting point) via route B_C using a die with a 90° square channel.

[†]Fine-grain structures are defined as those having a mean grain size of ~1 to 10 μm .

This resulted in a well-recrystallized material with a mean grain size of 3 μm and a minor fraction of nano-scale precipitates of the Al_2LiMg and $\text{Al}_3(\text{Li}, \text{Zr})$ phases evenly distributed within the interior of grains (supplementary Fig. S1). The processing procedures and resulting microstructure are described in more detail elsewhere [64].

Tension specimens for superplasticity tests were machined along the longitudinal axis of the ECAP'ed billet; they had a gage (reduced) section measuring $5 \times 3 \times 0.8 \text{ mm}^3$. The specimens were mechanically polished to achieve a uniform thickness and to remove surface defects. Tension tests were conducted to failure at 320°C ($0.64T_m$), 355°C ($0.67T_m$), 370°C ($0.69T_m$), and 395°C ($0.72T_m$). As shown in previous work [65], this temperature interval covers the entire range of superplasticity for the 1420 alloy in the fine-grain condition. In all cases, tests were performed at a constant crosshead speed corresponding to a nominal strain rate of $3 \times 10^{-2} \text{ s}^{-1}$ using an Instron testing machine. As found previously [66], this particular strain rate provided the highest elongation to failure over the entire range of temperature which was investigated. Prior to each experiment, the test specimen was held at temperature for 10 min to attain thermal equilibrium. Furthermore, to enhance ductility, tensile straining was assisted by imposing ultrasonic vibration at a frequency of 20 kHz and amplitude of 5 μm by using in-house acoustic system [67]. As shown by Myshlyayev, et al. [67], this approach provided an ~60-pct. increase in elongation-to-failure due to the enhancement of diffusion-driven processes.

Selected rate-jump tests to determine values of the strain-rate sensitivity parameter (m) were also conducted by cycling the strain rate between 3×10^{-2} and $6 \times 10^{-2} \text{ s}^{-1}$ during tension testing over a true strain interval of 0.2 to 1.1.

Following tension testing, microstructure observations were performed using EBSD. To produce a suitable surface finish, each specimen was mounted and mechanically polished using conventional metallographic procedures followed by a final step comprising 24-h vibratory polishing with a suspension of colloidal silica. EBSD was then conducted using a

Hitachi S-4300SE field-emission-gun scanning electron microscope (FEG-SEM) operated at an accelerating voltage of 25 kV, which was equipped with a TSL OIM™ EBSD system. To investigate microstructure evolution at different length scales, EBSD maps were acquired for each material condition using a scan step size of 0.2 μm, 0.5 μm, or 2 μm. To improve the reliability of the acquired EBSD data, small grains comprising 3 or fewer pixels were automatically “cleaned” using the standard grain-dilation option of the EBSD software. Due to the limited angular accuracy of EBSD, boundaries with misorientations below 2° were excluded from consideration. Last, a 15° threshold was applied to differentiate low-angle boundaries (LABs) and high-angle grain boundaries (HAGBs).

3. Results

3.1. Mechanical behavior

Typical engineering stress-strain curves recorded during the tension tests (Fig. 1a) revealed that the total elongation to failure exceeded 400% (or a true failure strain ≥ 1.6) over the entire range of test temperatures. Thus, from a phenomenological standpoint, the studied alloy exhibited superplastic behavior. As expected, an increase in the test temperature resulted in a reduction of flow stress and promoted material ductility (Fig. 1a).

The corresponding true stress-true strain curves[‡] (Fig. 1b) showed a complex character. In all cases, it was characterized by pronounced strain hardening, the attainment of a peak, and finally what appeared to be flow softening. As described below, the observed strain hardening was associated with extensive intragranular slip activity and/or dynamic grain growth, thus being in the line with previous results reported in the literature [e.g. 1, 45-57]. Furthermore, steady-state flow was not observed. This behavior also agreed well with previous studies of superplastic behavior of the examined material [65, 67].

[‡]To compensate for the continuous decrease in true strain rate during tension testing, the true stress-true strain curves were corrected by multiplying each stress data point by a factor of $(L/L_0)^m$, where L denotes the instantaneous gage-section length, L_0 is the initial gage length, and m is the strain rate sensitivity.

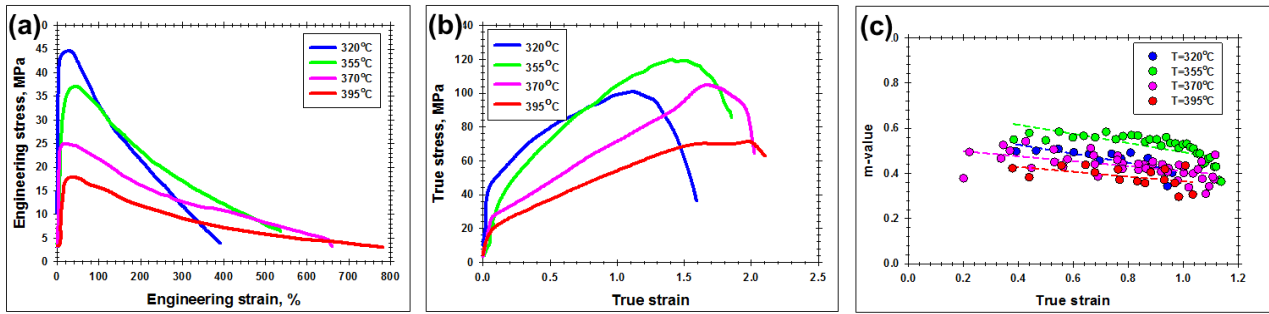


Figure 1. Effect of deformation temperature on tension behavior: (a) Engineering stress-strain curves, (b) true stress-true strain curves, and (c) the evolution of m -value with strain

The strain-rate-sensitivity parameter (m -value) provided additional insight into material behavior. Typical results are shown in Fig. 1c. In agreement with previous work [67], the m -value varied between 0.4 and 0.6, thus confirming the superplastic character of material flow. In addition, the strain-rate-sensitivity tended to *decrease* with superplastic strain. The possible origin of this interesting phenomenon is discussed in Section 4.3.

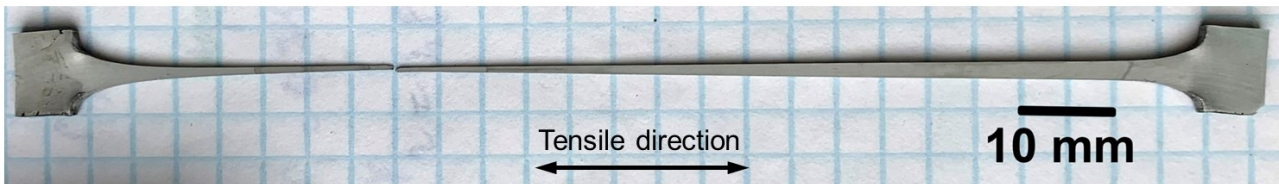


Figure 2. Typical appearance of a failed tension specimen, which was tested at 370°C

In addition to the relatively high m -value, experimental observations of failed specimens exhibited evidence of diffuse necking (e.g., Fig. 2). It is likely therefore, that the apparent flow softening at high strains observed in the true stress-strain curves (Fig. 1b) was associated with strain localization. The assumption of uniform flow in the gage section during the reduction of load-stroke data at high strains (i.e., at which extensive diffuse necking occurs) gives rise to such trends. Therefore, the apparent softening at high strains is *not* an intrinsic material-flow characteristic, but is rather an artifact of the data-analysis method. In superplasticity, this effect is sometimes referred to as “geometric softening” [68].

3.2. Effect of static annealing on microstructure evolution at superplastic temperatures

Due to the relatively-large grain-boundary area (and thus comparatively high grain-boundary energy), fine-grain materials are well known to be unstable at high temperatures and may experience marked microstructural coarsening. To separate the influence of thermal exposure from superplastic deformation, microstructure changes in the grip section of tested specimens were examined. In order to evaluate the extent of the static-annealing effect, the specimen strained at the highest superplastic temperature of 395°C was considered in the present work (Fig. 3).

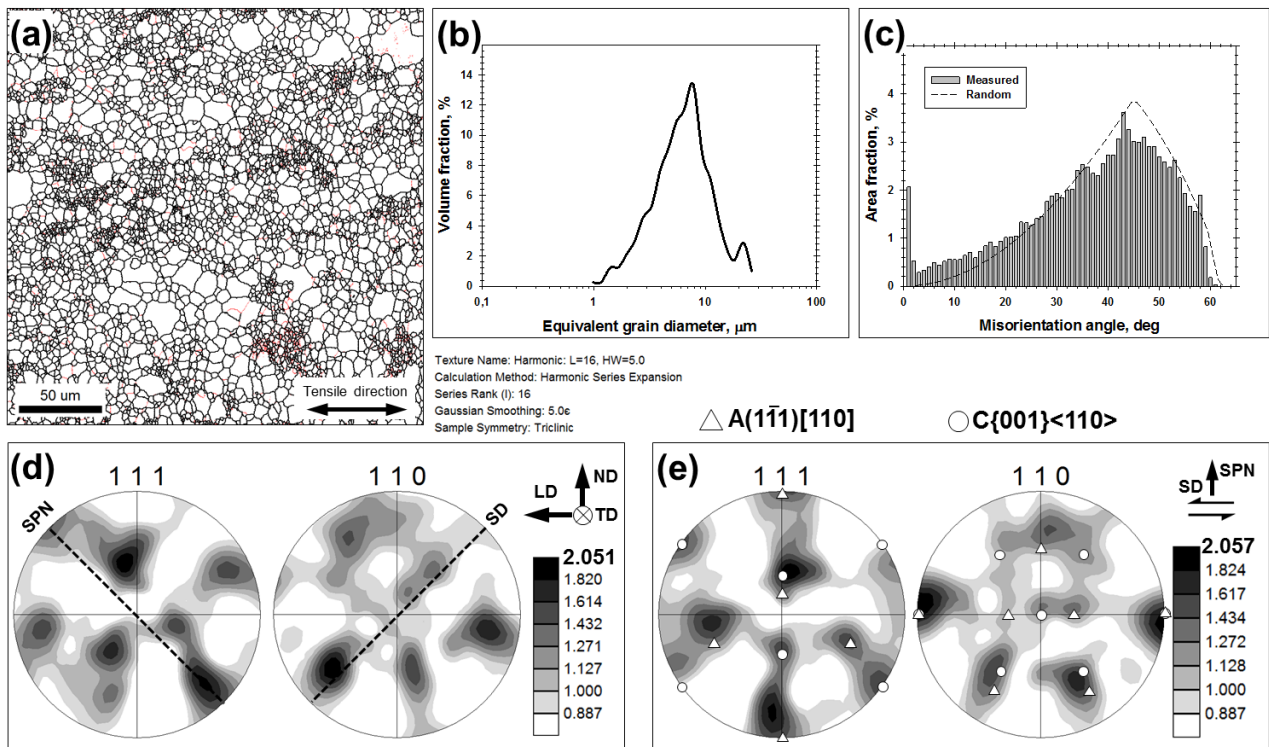


Figure 3. Microstructure evolution in the grip section of a specimen tested at 395°C: (a) EBSD grain-boundary map, (b) grain-size distribution, (c) misorientation-angle distribution, (d) measured 111 and 110 pole figures, and (e) rotated pole figures. LD, TD, ND, SPN, and SD denote the longitudinal direction, transverse direction, normal direction, shear plane normal, and shear direction of the ECAP billet, respectively. In (a), LABs and HAGB are depicted as red and black lines, respectively. In (d), dotted lines indicate the presumed orientations of the shear plane normal and shear direction. In (e), the positions of the ideal A ($(1\bar{1}1)[110]$) and C ($\{001\}\langle 110\rangle$) simple-shear orientations are shown.

It was found that the initial reasonably-homogeneous fine-grain microstructure evolved into a bimodal one (Fig. 3a). Although “islands” of the original 3- μm grains were still seen, the microstructure became dominated by much coarser grains, and the mean grain size was $\sim 9 \mu\text{m}$ (Fig. 3b); i.e., it was approximately tripled. The specific non-uniform morphology of the microstructure suggested that the material had experienced abnormal-like grain growth. Nevertheless, the material still contained a large fraction of LABs (Fig. 3c), which were preferentially concentrated in the surviving fine-grain remnants (red lines in Fig. 3a).

The corresponding texture changes were elucidated by 111 and 110 pole figures derived from EBSD measurements (Fig. 3d). For clarity, the orientations of the shear direction (SD) and the shear plane normal (SPN) characterizing deformation during ECAP [69] were superimposed on the pole figures. In addition, the pole figures were rotated to align the shear direction horizontally and the shear-plane normal vertically to simplify texture interpretation, as is typically done when analyzing simple-shear textures [69]. The textures indicated by the rotated pole figures (Fig. 3e) were relatively weak and diffuse but did exhibit clear signs of the simple-shear orientations $A(1\bar{1}1)[110]$ and $C\{001\}\langle 110\rangle$.

3.3. Microstructure changes in the reduced section

3.3.1. Microstructure morphology and grain size

EBSD measurements from the deformed, reduced sections of failed specimens also provided insight into microstructural changes during superplastic deformation. Typical examples are shown in Fig. 4, while the relevant microstructure statistics are summarized in Fig. 5. Material strained at a relatively low temperature exhibited a clearly-bimodal microstructure (Fig. 4a) with the fine grains clustered together in “islands” aligned parallel to the tension direction. With an increase in test temperature, the isolated bands of fine grains tended to disappear (Figs. 4b-d, Fig. 5a). On the other hand, the coarse-grain constituent

essentially increased in size (Figs. 4 and 5b-c), thus indicating the occurrence of dynamic grain growth.

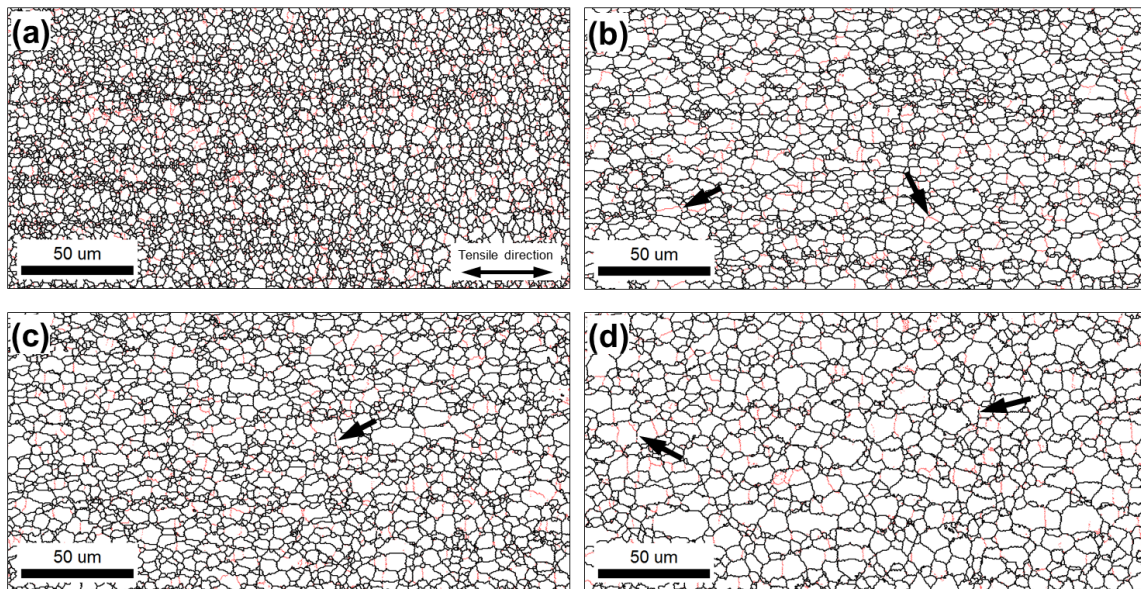


Figure 4. Selected portions of EBSD grain-boundary maps showing the microstructure in the gage section of failed specimens as a function of deformation temperature: (a) 320°C (elongation to failure = 469%), (b) 355°C (elongation to failure = 599%), (c) 370°C (elongation to failure = 894%), and (d) 395°C (elongation to failure = 988%). In all cases, LABs and HAGBs are depicted as red and black lines, respectively. Note: The tensile direction for all EBSD maps is shown in the bottom right corner of (a).

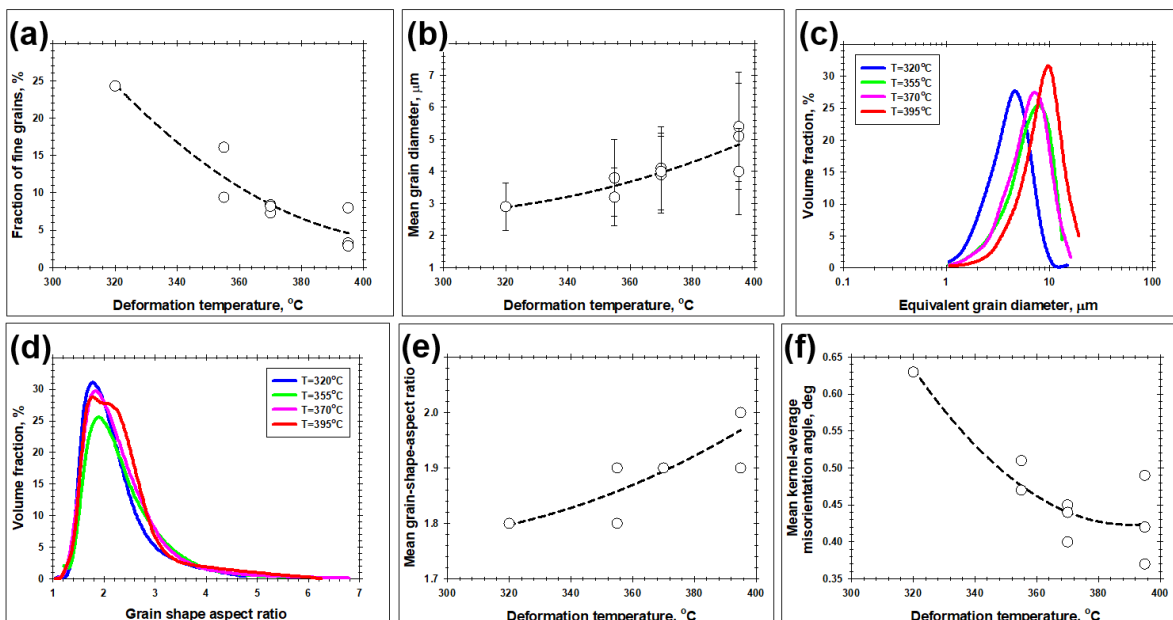


Figure 5. Effect of deformation temperature on (a) Fraction of fine grains, (b) mean grain size, (c) grain-size distribution, (d) grain-shape aspect-ratio distribution, (e) mean grain-shape aspect ratio, (f) mean kernel-average misorientation. In (b), error bars show the standard deviation

Although the microstructures appeared to be nearly equiaxed from a broad perspective (Fig. 4), quantitative analysis did reveal the presence of highly-elongated grains (Fig. 5d[§]). Moreover, the mean grain-shape aspect ratio exhibited a small but measurable increase with test temperature (Fig. 5e). In this context, it is important to emphasize that the elongated grains often contained LABs which were oriented approximately transverse to the tension axis (Fig. 4). Furthermore, these LABs were often characterized by a variable misorientation along their length with some adjacent segments being in the high-angle range; several examples are indicated by arrows in Fig. 4. These observations suggested that the apparently-equiaxed microstructure may have originated from the transverse subdivision of elongated grains, i.e., via a progressive process such as continuous dynamic recrystallization (CDRX). Such observations and conclusions imply that extensive intragranular slip occurred, as has been suggested by other data in the literature [45-57].

3.3.2. Evaluation of dislocation substructure

Further insight into intragranular slip activity was obtained from misorientations within grains, which were quantified using the kernel-average misorientation (KAM)** feature of the EBSD software. Typical KAM maps (Fig. 6) revealed several important aspects of the superplastic deformation.

First and foremost, a very noticeable variation of KAM was found within grains. This observation implied the evolution of substructure and hence substantial dislocation activity. This finding is in agreement with several previous works in the scientific literature [10, 45-57, 70]. In the present research, the most pronounced levels of KAM were often seen

[§]In this work, the grain-shape aspect ratio was defined as the length of the major axis divided by the length of the minor axis of the ellipse fitted to each grain.

**The KAM, or kernel-average misorientation, comprises the average misorientation around each pixel in an EBSD map with respect to its nearest-neighbor pixels.

near grain boundaries and at triple joints (Fig. 6). Another significant finding was the relatively-high KAM values revealed within the fine-grain remnants of the original

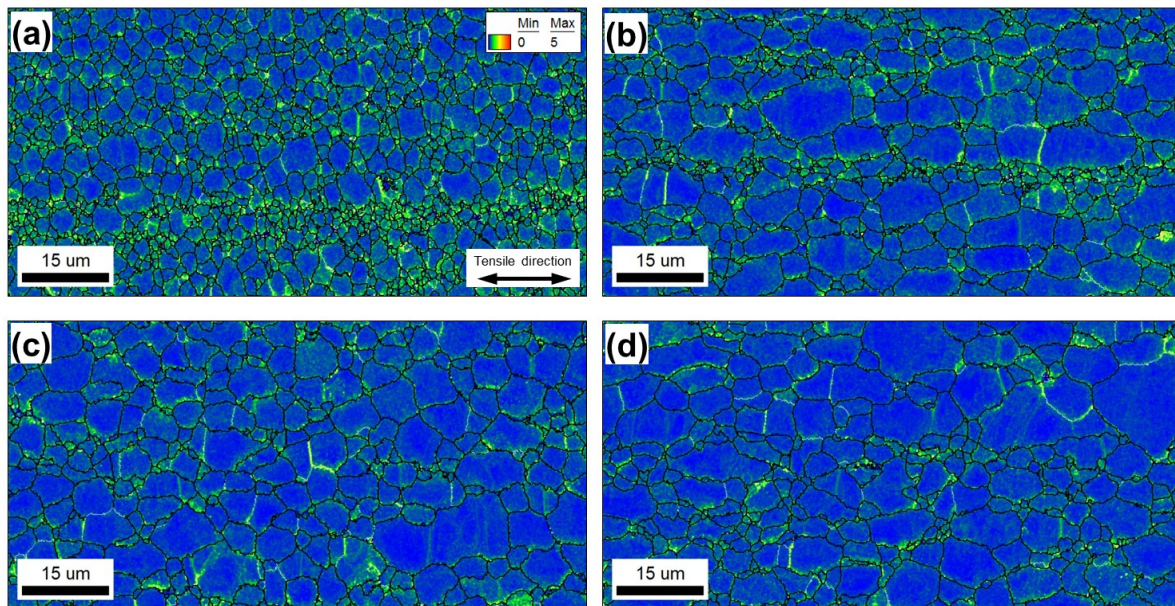


Figure 6. Selected portions of EBSD kernel-average-misorientation (KAM) maps reflecting the dislocation structure in the gage section of specimens pulled in tension at (a) 320°C, (b) 355°C, (c) 370°C, or (d) 395°C. The KAM color code is shown in the top right corner of (a). In all cases, LABs and HAGBs are depicted as white and black lines, respectively. Note: The tensile direction for all EBSD maps is shown in the bottom right corner of (a).

(as-ECAPed) microstructure (Figs. 6a, b). This observation is discussed in Section 3.4. In accordance with expectations, the KAM value tended to decrease with superplastic temperature (Figs. 5f and 6a to d).

3.3.3. Texture and misorientation distribution

The evolution of texture and the misorientation distributions within the reduced section further illuminated microstructure changes during superplastic deformation. A typical inverse-pole figure (IPF) for the tension direction (Fig. 7a) showed that the texture was very weak with a peak intensity of only ~1.5 times random and a preference of $\{hkl\}\langle 100 \rangle$ and $\{hkl\}\langle 111 \rangle$ fiber orientations. Both these texture components normally develop during axial tension of aluminum alloys [e.g. 71].

Typical misorientation-angle and misorientation-axis distributions (Figs. 7b and c, respectively) were both close to random, except for a substantial LAB fraction in Fig. 7b. Considering the sub-boundary structure suggested by the KAM maps (Fig. 6), it seems

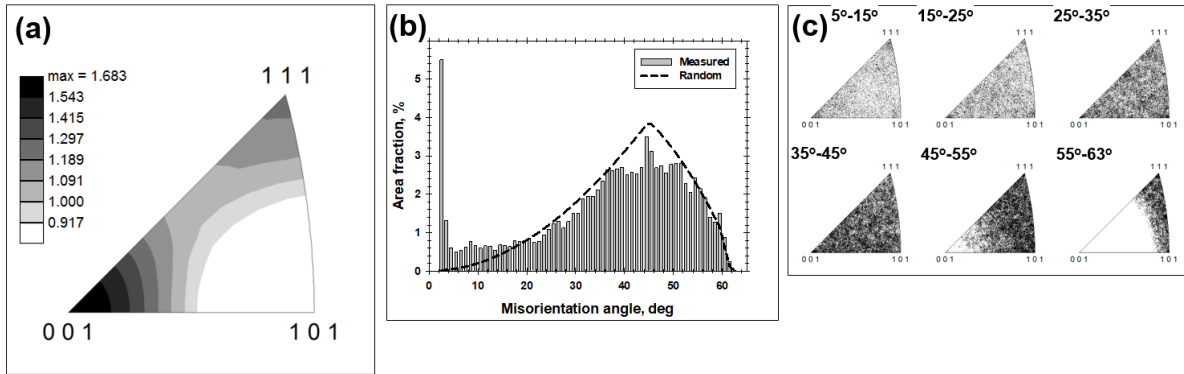


Figure 7. Typical results for (a) an inverse-pole figure showing the grain orientation relative to the tension direction, (b) the misorientation-angle distribution, and (c) the misorientation-axis distributions derived from EBSD maps taken from the gage section of failed specimens tested at 370°C

likely that the actual fractions of LABs were larger than those measured. Despite such uncertainty, however, the formation of distinct crystallographic texture and the presence of a noticeable fraction of LABs both suggested significant activity of intragranular slip.

3.4. Superplastic behavior of fine-grain microstructure

The development of a bimodal grain size at low superplastic temperatures (Fig. 4a) provided an opportunity to investigate the superplastic behavior of the original fine grains. According to the well-accepted view, such microstructures are particularly suitable for the accommodation of imposed deformation via grain-boundary sliding. This mechanism implies a motion of grains relative each other which thus result in a change of neighbors. In this context, it was of particular interest that the fine, superplastically-strained grains tended to cluster together (Fig. 4a), rather than intermix with the coarser grains, as might be expected for classical grain-boundary sliding.

To provide quantitative insight into the deformation mechanism of the fine-grained microstructure, EBSD data were partitioned into fine-grain and coarse-grain constituents

using a threshold grain size of 3 μm , as exemplified in Fig. 8. In order to obtain the highest measurement statistics for the fine-grained microstructure, the partitioning approach was applied to the data taken from the specimen strained at the lowest superplastic temperature of 320°C. The relevant results are summarized in Figs. 9 and 10.

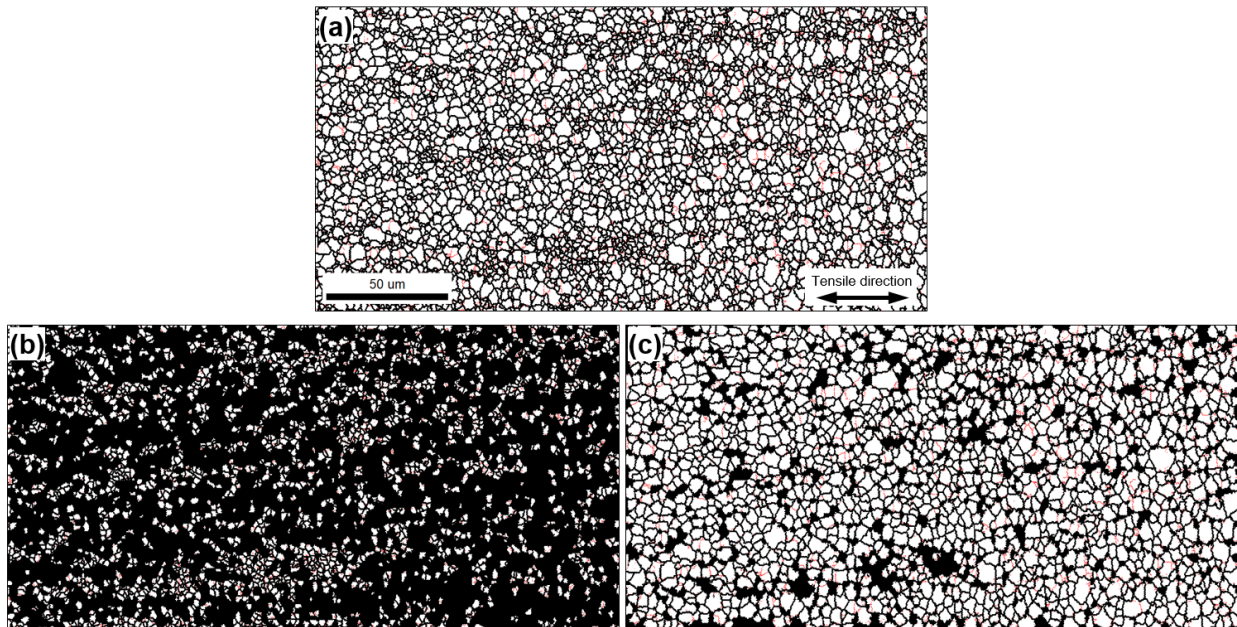


Figure 8. Microstructure partitioning in material tested at 320°C: (a) Entire EBSD grain-boundary map, (b) fine-grain microstructure constituent (grain size $\leq 3 \mu\text{m}$), and (c) coarse-grain microstructure constituent (grain size $> 3 \mu\text{m}$). In all cases, LABs and HAGBs are depicted as red and black lines, respectively. Note: The tensile direction for all EBSD maps is shown in the bottom right corner of (a).

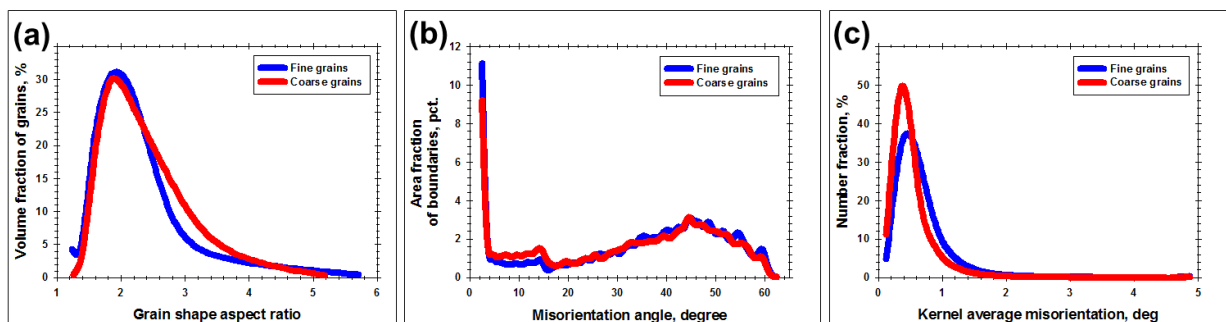


Figure 9. Comparison of microstructure characteristics measured in the fine-grain and coarse-grain areas of material deformed in tension at 320°C: (a) Grain-shape aspect-ratio distribution, (b) misorientation-angle distribution, and (c) kernel-average-misorientation distribution

Although the fine grains typically had a nearly-equiaxed shape, the grain-shape aspect ratio was measured in some cases to be as high as ~ 5.5 (Fig. 9a). Also, it was found that

the fine-grain regions contained a relatively-large fraction of LABs (Fig. 9b) and were characterized by comparatively-high values of KAM (Fig. 9c). The latter observation was

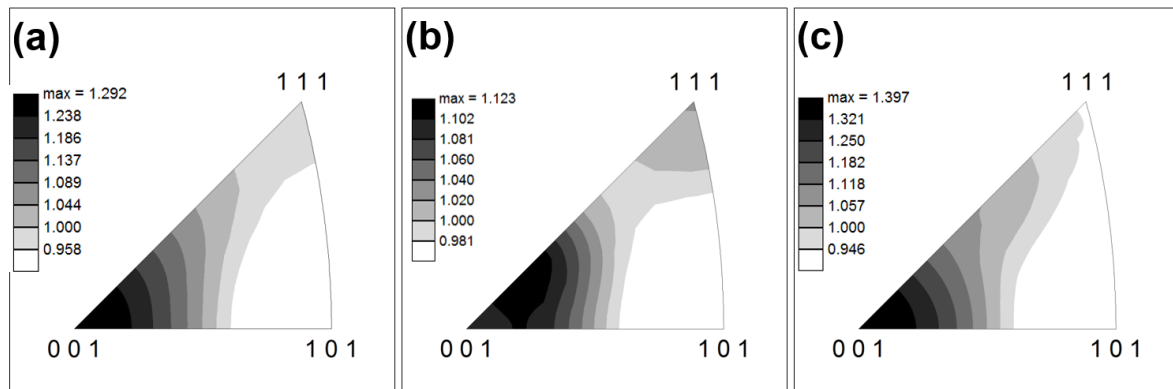


Figure 10. Inverse pole figures for the tension direction for material deformed at 320°C: (a) Entire data set, (b) fine-grain microstructural constituent, and (c) coarse-grain microstructural constituent.

consistent with the KAM map in Fig. 6a, and thus supported the conclusion regarding the generation of a relatively-high dislocation density. Moreover, the partitioning of the global texture in Fig. 10a revealed a slightly-higher intensity of the $\{hk\ell\}\langle 111\rangle$ fiber in the fine-grain domains (compare Figs. 10b and 10c). This suggested increased activity of cross slip. Taken together, the above results provided evidence of extensive intragranular slip in the fine-grain regions.

4. Discussion

True stress-true strain curves and m-value measurements (Fig. 1b and c, respectively) suggested that superplastic deformation was a relatively-complex process which involved several different stages. This complicates interpretation of the underlying microstructural mechanisms. Nevertheless, several important observations can be made and those are discussed in the following subsections.

4.1. Microstructure coarsening and intragranular slip

The microstructure data in Section 3 provided strong evidence of the operation of at least two mechanisms of microstructure evolution during superplastic deformation: grain

growth and intragranular slip^{††}. This result agrees well with the conventional concept of superplastic deformation.

The initial stage of grain growth appeared to be abnormal-like, i.e., involving a small subset of so-called “rogue” grains which possessed a growth advantage due to non-uniformity in stored work, texture, etc. (Figs. 3a and 4a). After elimination of the original fine-grain structure, however, microstructure coarsening appeared to become normal in nature (Figs. 4b-d and 5c). The reason for this unusual behavior is not clear and warrants further study. However, the possible influence of impingement of abnormal grains, pinning by remnant fine grains, etc, seems to provide several plausible sources for the transition from abnormal-like to normal behavior.

The various experimental observations, including noticeable strain hardening (Fig. 1b) and grain elongation (Fig. 5e), the formation of the pronounced substructure in grain interiors (Fig. 6), and the development of crystallographic texture (Fig. 7a), provided strong evidence of extensive intragranular slip (concurrent with grain growth) over the entire range of temperature used in the present work. Moreover, the transverse orientation of LABs relative to the tension direction (Fig. 4) and the observed LAB-to-HAGB transformations (arrows in Fig. 4) suggested the operation of continuous dynamic recrystallization. The activation of this mechanism may eventually give rise the apparently equiaxed final grains and thus may explain the observed microstructure morphology.

It is also noteworthy that coarse-grain materials can exhibit relatively high rates of strain hardening due to the prevalence of intragranular slip. In the present context, the extended strain hardening stage observed at 370°C and 395°C in the present work (Fig.

^{††} From ThermoCalc calculations, it was predicted that the fraction of second-phase constituent particles changed noticeably during heating to the test temperatures (supplementary Fig. S2). Such changes may exert an influence on superplastic behavior. The clarification of this influence, however, requires additional quantitative study.

1b) was presumably attributable, at least partially, to considerable grain growth occurring at these temperatures (Figs. 4c-d, and 5b-c).

It is also of note that the material used in the present work contained a relatively-high concentration of magnesium. It is sometimes believed that this solute may enhance self-diffusion in aluminum alloys [72] (and thus promote intragranular slip) but retard grain growth via segregation at grain boundaries [28]. Both these factors may contribute to the relatively-high ductility observed in the present study.

4.2. Continuous dynamic recrystallization vs grain boundary sliding

According to the classical core-mantle superplasticity model, grain-boundary sliding normally results in stress concentrations at triple joints which are relaxed by appropriate intragranular slip [73]. Hence, the substructure observed in grain interiors in the present study (Figs. 4 and 6) may originate from such accommodation slip. Therefore, to evaluate the significance of the intragranular slip activity for superplastic flow, a quantitative approach is necessary.

As suggested above, the nearly equiaxed microstructure observed in the present study could be associated with the progressive development of continuous dynamic recrystallization. In the present work, the process involved the transverse subdivision of elongated grains which finally transformed into chains of low-aspect-ratio grains. If this was indeed the case, some orientation relationship between the grains within such chains may have been retained [1]. On the other hand, if grain-boundary sliding was the dominant microstructural process, the concomitant grain intermixing/rotations would likely have destroyed any orientation relationship between neighboring grains. The opposing trends associated with two mechanisms thus provide an opportunity to evaluate their contributions to superplastic flow.

EBSD texture maps calculated for different test temperatures (Fig. 11) revealed the extent of a possible orientation relationship between the neighboring grains. In these maps,

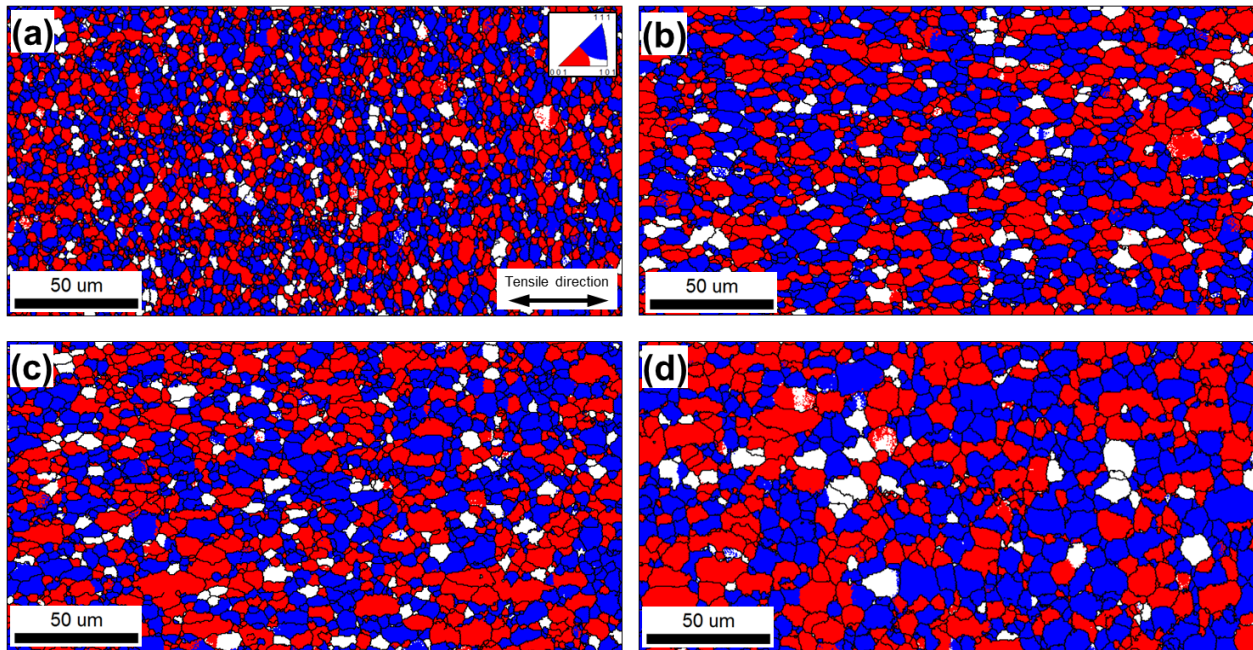


Figure 11. EBSD texture maps showing the orientation relationship between neighboring grains in material deformed in tension at (a) 320°C, (b) 355°C, (c) 370°C, or (d) 395°C. In the maps, the $\{hkl\}\langle 100 \rangle$ fiber texture (red color) and $\{hkl\}\langle 111 \rangle$ fiber texture (blue color) are shown for a 30-degree tolerance. For simplicity, the deviation from the ideal orientation is indicated in the standard stereographic triangle in the top right corner of (a). Note: The tensile direction for all EBSD maps is shown in the bottom right corner of (a).

the spatial distribution of two main texture components, i.e., $\{hkl\}\langle 100 \rangle$ (in red) and $\{hkl\}\langle 111 \rangle$ (in blue), were shown. A relatively large, 30° orientation tolerance was used for each texture component. Accordingly, these two orientations covered almost the entire orientation space as shown in the standard stereographic triangle in the top right corner of Fig. 11a. The results shown in Figs. 11a to d indicated that grains belonging to the same texture component (i.e., either $\{hkl\}\langle 100 \rangle$ or $\{hkl\}\langle 111 \rangle$) often clustered together. In some cases, they formed chains aligned with tension axis. Presumably, this does indicate that an orientation relationship did exist, and the nearly-equiaxed microstructure had indeed originated from transverse subdivision of coarser pre-elongated grains.

In this context, it is of interest to quantify the macro-scale deformation associated with grain elongation (i.e., elongation via intragranular slip). Accordingly, the grain-shape aspect ratio of the pre-elongated grains was evaluated from Fig. 11. Manual measurements showed that this quantity never exceed 10. Assuming that the grains elongated in

proportion of the tensile strain, it can readily be shown that the macro-scale engineering strain e and the grain-shape aspect ratio λ are related as $e \approx (\lambda^{2/3} - 1) \times 100\%$ (Appendix). Hence, a grain-shape aspect ratio of 10 reflects a tensile elongation of only ~364%. In some cases, this was considerably lower than the measured values of total elongation to failure (Fig. 1a). In these instances, therefore, it can be surmised that grain-boundary sliding also contributed to the overall ductility.

It is important to emphasize that the above simple relationship between the engineering strain and grain elongation accounts for neither dynamic grain growth nor continuous recrystallization which occurred during the tension tests. Both these processes would tend to *reduce* the grain-shape aspect ratio. Thus, the real contribution of intragranular slip was likely higher than the calculated one.

4.3. Temperature effect

At the relatively-low test temperatures of 320°C (0.64 T_m) and 350°C (0.67 T_m), the measured elongation to failure (Fig. 1a) was reasonably close to that predicted in the previous section. This implied that intragranular slip may have dominated superplastic flow, which could have led to relatively-high flow stresses at these temperatures (Fig. 1b). Moreover, it was also consistent with preferential clustering of the fine-grain remnants observed at these temperatures (Figs. 4a and b). At higher temperatures, by contrast, the measured strains exceeded the predicted one, and the flow was characterized by very low flow stresses (Fig. 1b). In addition, the fine grains were found to be distributed in a nearly-random fashion throughout the microstructure (Figs. 4c and d). Hence, material flow at 370°C and 395°C was likely measurably influenced by grain-boundary sliding as well.

It is worth noting that the extent of grain-boundary sliding is normally reduced by grain growth. In this context, the measured *decrease* of m-value with increasing strain (Fig. 1c) was likely associated with noticeable microstructural coarsening at high deformation

temperatures (Figs. 5b and c). Hence, it is quite possible that the specific contributions of different mechanisms to the global material flow varied noticeably during superplastic deformation. **If so, the conclusions reached in the present section are oversimplified. Therefore, a more-detailed investigation of microstructure evolution during superplastic flow is necessary.**

5. Conclusions

In this work, EBSD was applied to investigate superplastic-flow behavior of an Al-Mg-Li alloy with an “ideal” fine-grain recrystallized microstructure. To this end, tension tests taken to failure were conducted at 320°C (0.64 T_m), 355°C (0.67 T_m), 370°C (0.69 T_m), and 395°C (0.72 T_m), and a nominal strain rate of $3 \times 10^{-2} \text{ s}^{-1}$. The main conclusions derived from this work are as follows.

1. The deformation response shows clear evidence of two microstructural processes: (i) Dynamic grain growth, and (ii) continuous dynamic recrystallization. The initial stages of grain growth exhibit an abnormal character and result in a bimodal grain structure. Continuous dynamic recrystallization involves a transverse subdivision of pre-elongated grains which eventually transform into chains of nearly-equiaxed grains.

2. A number of pieces of experimental data, including a high rate of strain hardening, noticeable grain elongation, the formation of pronounced substructure within grain interiors, and the development of crystallographic texture, provide evidence of extensive intragranular slip over the entire range of temperature investigated in this work. At 320°C and 355°C, this mechanism appears to play a dominant role in superplastic flow. At higher temperatures, on the other hand, the contribution of intragranular slip appears to be insufficient to accommodate the macro-scale strain, and therefore material flow is likely influenced measurably by grain-boundary sliding as well.

Appendix. Relationship between engineering strain and grain shape aspect ratio

Assume that an original cube-shaped grain had experienced an axial tension along its characteristic dimension “a” thus transforming into a parallelepiped-shaped grain of characteristic sizes of $L \times b \times b$ (Fig. A1).

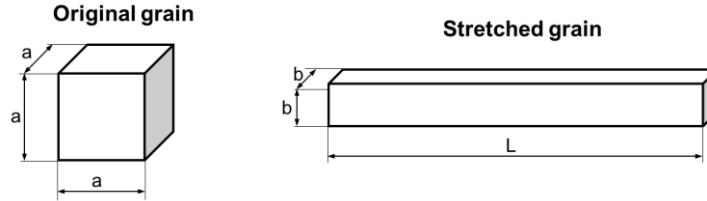


Figure A1. Schematic showing a change of grain shape during uniaxial tension

Per definition, the grain shape aspect ratio of the stretched grain is $\lambda = L/b$, and the applied engineering strain is $e = \frac{L-a}{a} \times 100\% = \left(\frac{L}{a} - 1\right) \times 100\%$. As the grain volume did not change, $a^3 = Lb^2$, i.e., $a = \sqrt[3]{Lb^2}$. Hence, the engineering strain can be expressed as

$$e = \left(\frac{L}{\sqrt[3]{Lb^2}} - 1\right) \times 100\% = \left(\sqrt[3]{\frac{L^3}{Lb^2}} - 1\right) \times 100\% = \left(\sqrt[3]{\frac{L^2}{b^2}} - 1\right) \times 100\% = \left(\sqrt[3]{\lambda^2} - 1\right) \times 100\%$$

Acknowledgements

M. Myshlyayev, S.Mironov, G. Korznikova, A. Aletdinov, G. Khalikova., T. Konkova, and E. Korznikova gratefully acknowledge financial support from the Russian Fund for Fundamental Research, project No.20-02-00331 A (for performing superplastic tension tests, microstructural observations, data analysis, and drafting of the manuscript). G. Raab was supported under the auspices of a Resolution of the Government of the Russian Federation, April 9, 2010, No. 220, Contract No. 075-15-2019-869 (for processing of the studied material).

Data availability

The raw/processed data required to reproduce these findings cannot be shared at this time inasmuch as the data are integral to an ongoing study

References

References

- [1] P.S. Bate, N. Ridley, B. Zhang, *Mechanical behavior and microstructural evolution in superplastic Al-Li-Mg-Cu-Zr AA8090*, *Acta Materialia* 55 (2007) 4995-5006; <https://doi.org/10.1016/j.actamat.2007.05.017>
- [2] Z. Liu, P. Li, L. Xiong, T. Liu, L. He, *High-temperature tensile deformation behavior and microstructure evolution of Ti55 titanium alloy*, *Mater. Sci. Eng. A680* (2017) 259-269; <https://doi.org/10.1016/j.msea.2016.10.095>
- [3] F.C. Liu, P. Xue, Z.Y. Ma, *Microstructural evolution in recrystallized and unrecrystallized Al-Mg-Sc alloys during superplastic deformation*, *Mater. Sci. Eng. A547* (2012) 55-63; <https://doi.org/10.1016/j.msea.2012.03.076>
- [4] R. Kaibyshev, A. Goloborodko, F. Musin, I. Nikulin, T. Sakai, *The role of grain boundary sliding in microstructural evolution during superplastic deformation of a 7055 aluminum alloy*, *Mater. Trans.* 43 (2002) 2408-2414; <https://doi.org/10.2320/matertrans.432408>
- [5] Y. Xun, M.J. Tan, T.G. Nieh, *Grain boundary characterization in superplastic deformation of Al-Li alloy using electron backscatter diffraction*, *Mater. Sci. Tech.* 20 (2004) 173-180; <https://doi.org/10.1179/174328413X13789824293786>
- [6] A.A. Kishchik, A.V. Mikhaylovskaya, A.D. Kotov, O.V. Rofman, V.K. Portnoy, *Al-Mg-Fe-Ni based alloy for high strain rate superplastic forming*, *Mater. Sci. Eng. A718* (2018) 190-197; <https://doi.org/10.1016/j.msea.2018.01.099>
- [7] T. Yasmeen, B. Zhao, J.-H. Zheng, F. Tian, J. Lin, J. Jiang, *The study of flow behavior and governing mechanisms of a titanium alloy during superplastic forming*, *Mater. Sci. Eng. A788* (2020) 139482; <https://doi.org/10.1016/j.msea.2020.139482>
- [8] C. Zhang, Y. Xiao, K. Ma, Y. Wang, Z. Liu, Z. Liu, W. Zhang, *Superplastic flow and deformation mechanism of the rolled Al-Mg-Li-Sc-Zr alloy with banded microstructure*, *Metals* 11 (2021) 404; <https://doi.org/10.3390/met11030404>
- [9] J. Li, X. Ren, X. Gao, *Effect of superplastic deformation on microstructure evolution of 3207 duplex stainless steel*, *Mater. Character.* 64 (2020) 110320; <https://doi.org/10.1016/j.matchar.2020.110320>

- [10] S.J. Hales, T.R. Mcnelley, *Microstructural evolution by continuous recrystallization in a superplastic Al-Mg alloy*, *Acta Metall.* 36 (1988) 1229-1239; [https://doi.org/10.1016/0001-6160\(88\)90275-1](https://doi.org/10.1016/0001-6160(88)90275-1)
- [11] X. Yang, H. Miura, T. Sakai, *Continuous dynamic recrystallization in a superplastic 7075 aluminum alloy*, *Mater. Trans.* 43 (2002) 2400-24007; <https://doi.org/10.2320/matertrans.43.2400>
- [12] K. Tsuzaki, H. Matsuyama, M. Nagao, T. Maki, *High-strain rate superplasticity and role of dynamic recrystallization in a superplastic duplex stainless steel*, *Mater. Trans.* 31 (1990) 983-994; <https://doi.org/10.2320/matertrans1989.31.983>
- [13] R.H. Bricknell, J.W. Edington, *Deformation characteristics of an Al-6Cu-0.4Zr superplastic alloy*, *Metall. Trans. A* 10 (1979) 1257-1263; <https://doi.org/10.1007/BF02811981>
- [14] J. Liu, D.J. Chakrabarti, *Grain structure and microtexture evolution during superplastic forming of a high strength Al-Zn-Mg-Cu alloy*, *Acta Mater.* 44 (1996) 4647-4661; [https://doi.org/10.1016/S1359-6454\(96\)00141-3](https://doi.org/10.1016/S1359-6454(96)00141-3)
- [15] R. Kaibyshev, T. Sakai, F. Musin, I. Nikulin, H. Miura, *Superplastic behavior of a 7055 aluminum alloy*, *Scripta Mater.* 45 (2001) 1373-1380; [https://doi.org/10.1016/S1359-6462\(01\)01172-1](https://doi.org/10.1016/S1359-6462(01)01172-1)
- [16] K. Higashi, J. Wolfenstine, *Microstructural evolution during superplastic flow of a binary Mg-8.5 wt.% Li alloy*, *Mater. Letter.* 10 (1991) 329-332; [https://doi.org/10.1016/0167-577X\(91\)90147-X](https://doi.org/10.1016/0167-577X(91)90147-X)
- [17] F. Sun, D. Lin, *Superplastic phenomenon in a large-grained TiAl alloy*, *Scripta Mater.* 44 (2001) 665-670; [https://doi.org/10.1016/S1359-6462\(00\)00635-7](https://doi.org/10.1016/S1359-6462(00)00635-7)
- [18] T.R. McNelley, M.E. McMahon, *Microtexture and grain boundary evolution during microstructural refinement processes in SUPRAL 2004*, *Metall. Mater. Trans. A* 28 (1997) 1879-1887; <https://doi.org/10.1007/s11661-997-0118-2>
- [19] E.-W. Lee, T.R. McNelley, *Microstructure evolution during processing and superplastic flow in a high magnesium Al-Mg alloy*, *Mater. Sci. Eng.* 93 (1987) 45-55; [https://doi.org/10.1016/0025-5416\(87\)90411-3](https://doi.org/10.1016/0025-5416(87)90411-3)
- [20] T. Hirata, T. Mukai, N. Saito, S. Tanabe, M. Kohzu, and K. Higashi, *Experimental prediction of deformation mechanisms after continuous dynamic recrystallization in superplastic P/M7474*, *J. Mater. Sci.* 38 (2003) 3925-3932; <https://doi.org/10.1023/A:1026146112559>
- [21] Z. Liu, P. Li, L. Geng, T. Liu, H. Gao, *Microstructure and texture evolution of TA32 titanium alloy during superplastic deformation*, *Mater. Sci. Eng. A* 699 (2017) 71-80; <https://doi.org/10.1016/j.msea.2017.05.082>
- [22] Y.L. Duan, L. Tang, Y. Deng, X.W. Cao, G.F. Xu, Z.M. Yin, *Superplastic behavior and microstructure evolution of a new Al-Mg-Sc-Zr alloy subjected to a simple thermomechanical processing*, *Mater. Sci. Eng. A* 669 (2016) 205-217; <https://doi.org/10.1016/j.msea.2016.05.086>

- [23] X. Zhang, M.J Tan, Dislocation model for continuous recrystallisation during Initial stage of superplastic deformation, *Scripta Mater.* 38 (1998) 827-831; [https://doi.org/10.1016/S1359-6462\(97\)00535-6](https://doi.org/10.1016/S1359-6462(97)00535-6)
- [24] X. Du, B. Wu, *Continuous dynamic recrystallization of extruded NiAl polycrystals during the superplastic deformation process*, *Metall. Mater. Trans. A* 36 (2005) 3343–3351; <https://doi.org/10.1007/s11661-005-0009-3>
- [25] D. Jiang, R. Liu, C. Wang, Z. Wang, and T. Imai, *Microstructure and superplasticity of an Al-Zn-Mg-Cu alloy*, *J. Mater. Sci.* 34 (1999) 3363–3366; <https://doi.org/10.1023/A:1004629031261>
- [26] Z. Cui, W. Zhong, J. Bao, P. Zhan, L. Yong, *Superplastic behavior at high strain rate of warm-rolled 2618A commercial aluminum alloy*, *Scripta Metall. Mater.* 31 (1994) 1311-1315, [https://doi.org/10.1016/0956-716X\(94\)90109-0](https://doi.org/10.1016/0956-716X(94)90109-0)
- [27] H. Park, B.C. De Cooman, *Creep-induced microstructure evolution of type 2205 duplex stainless steel during continuous annealing processing*, *Steel Res. Int.* 85 (2014) 756-770; <https://doi.org/10.1002/srin.201300142>
- [28] M. Zha, H. Zhang, H. Jia, Y. Gao, S. Jin, G. Sha, R. Bjorge, R.H. Mathiesen, H.J. Roven, H. Wang, Y. Li, *Prominent role of multi-scale microstructural heterogeneities on superplastic deformation of a high solid solution Al–7Mg alloy*, *Int. J. Plast.* 146 (2021) 103108; <https://doi.org/10.1016/j.ijplas.2021.103108>
- [29] D. Lin, J. Hu, D. Jiang, *Superplasticity of Ni-rich single phase NiAl intermetallics with large grains*, *Intermetallics* 13 (2005) 343-349; <https://doi.org/10.1016/j.intermet.2004.07.008>.
- [30] J. Hu, D. Lin, *Microstructural evolution of superplasticity in large-grained Ni–48Al intermetallics*, *Mater. Sci. Eng. A*371 (2004) 113-118; <https://doi.org/10.1016/j.msea.2003.10.245>
- [31] H. Xie, D. Lin, Y. Chai, J. Hu, *EBSD investigation on the evolution of microstructure and grain boundaries in coarse-grained Ni–48Al upon large deformation at elevated temperature*, *Intermetallics* 58 (2015) 98-102; <https://doi.org/10.1016/j.intermet.2014.12.003>.
- [32] D. Jiang, D. Lin, *The microstructural evolution in large-grained Ni–40Al during superplastic deformation*, *J. Alloys Compd.* 415 (2006) 177-181; <https://doi.org/10.1016/j.jallcom.2005.08.013>
- [33] D. Lin, D. Li, Y. Liu, *Superplasticity in large-grained FeAl-based intermetallic alloys*, *Intermetallics*, 6 (1998) 243-256, [https://doi.org/10.1016/S0966-9795\(97\)00072-1](https://doi.org/10.1016/S0966-9795(97)00072-1)
- [34] D. Lin, Y. Liu, *Microstructural evolution and mechanisms of superplasticity in large-grained iron aluminides*, *Mater. Sci. Eng. A* 268 (1999) 83-89; [https://doi.org/10.1016/S0921-5093\(99\)00080-5](https://doi.org/10.1016/S0921-5093(99)00080-5)
- [35] D. Lin, F. Sun, *Superplasticity in a large-grained TiAl alloy*, *Intermetallics* 12 (2004) 875-883; <https://doi.org/10.1016/j.intermet.2004.02.039>

- [36] J. Hu, D. Lin, *Superplasticity of single phase Ni–42Al intermetallics with large grains*, Mater. Sci. Eng. A 441 (2006) 142-148; <https://doi.org/10.1016/j.msea.2006.08.011>
- [37] D. Lin, Y. Liu, *An electron back-scattered diffraction study on the microstructural evolution in large-grained iron aluminides during superplastic deformation*, Mater. Sci. Eng. A 329–331 (2002) 863-871; [https://doi.org/10.1016/S0921-5093\(01\)01643-4](https://doi.org/10.1016/S0921-5093(01)01643-4)
- [38] J.P. Chu, H.Y. Yasuda, Y. Umakoshi, K. Inoue, *Electron backscattered diffraction study on superplastic coarse-grained Fe–27 at.%Al: processing effects*, Intermetallics 8 (2000) 1075-1079; [https://doi.org/10.1016/S0966-9795\(00\)00032-7](https://doi.org/10.1016/S0966-9795(00)00032-7)
- [39] X. Zhang, W. Zeng, Y. Li, B. Jiao, Z. Yuan, Y. Chen, Z. Sun, *The superplasticity and microstructure evolution of coarse-grained Ti40 alloy*, Mater. Sci. Technol. 33 (2017) 1919-1925; <https://doi.org/10.1080/02670836.2017.1337289>
- [40] H.Z. Niu, F.T. Kong, Y.Y. Chen, C.J. Zhang, *Low-temperature superplasticity of forged Ti–43Al–4Nb–2Mo–0.5B alloy*, J. Alloys Compd. 543 (2012) 19-25; <https://doi.org/10.1016/j.jallcom.2012.07.127>
- [41] L.H. Wu, B.L. Xiao, D.R. Ni, Z.Y. Ma, X.H. Li, M.J. Fu, Y.S. Zeng, *Achieving superior superplasticity from lamellar microstructure of a nugget in a friction-stir welded Ti-6Al-4V joint*, Scripta Mater. 98 (2015) 44–47; <http://dx.doi.org/10.1016/j.scriptamat.2014.11.011>
- [42] W. Zhang, H. Liu, H. Ding, H. Fujii, *Superplastic deformation mechanism of the friction stir processed fully lamellar Ti-6Al-4V alloy*, Mater. Sci. Eng. A 785 (2020) 139390; <https://doi.org/10.1016/j.msea.2020.139390>
- [43] H.-M. Zhang, X.-M. Cheng, M. Zha, Y.-K. Li, C. Wang, Z.-Z. Yang, J.-G. Wang, H.-Y. Wang, *A superplastic bimodal grain-structured Mg–9Al–1Zn alloy processed by short-process hard-plate rolling*, Mater. 8 (2019) 100443; <https://doi.org/10.1016/j.mtla.2019.100443>
- [44] X. Li, Q. Le, D. Li, P. Wang, P. Jin, C. Cheng, X. Chen, L. Ren, *Hot tensile deformation behavior of extruded LAZ532 alloy with heterostructure*, Mater. Sci. Eng. A 801 (2021) 140412; <https://doi.org/10.1016/j.msea.2020.140412>
- [45] K. Tsuzaki, Xiaoxu Huang, T. Maki, *Mechanism of dynamic continuous recrystallization during superplastic deformation in a microduplex stainless steel*, Acta Mater. 44 (1996) 4491-4499; [https://doi.org/10.1016/1359-6454\(96\)00080-8](https://doi.org/10.1016/1359-6454(96)00080-8)
- [46] L. Qing, H. Xiaoxu, Y. Mei, Y. Jinfeng, *On deformation-induced continuous recrystallization in a superplastic Al-Li-Cu-Mg-Zr alloy*, Acta Metal. Mater. 40 (1992) 1753-1762; [https://doi.org/10.1016/0956-7151\(92\)90118-X](https://doi.org/10.1016/0956-7151(92)90118-X)
- [47] C.F. Martin, J.J. Blandin, L. Salvo, *Variations in microstructure and texture during high temperature deformation of Al–Mg alloy*, Mater. Sci. Eng. A 297 (2001) 212-222; [https://doi.org/10.1016/S0921-5093\(00\)01260-0](https://doi.org/10.1016/S0921-5093(00)01260-0)

- [48] W. Zhang, H. Liu, H. Ding, H. Fujii, *Grain refinement and superplastic flow in friction stir processed Ti-15V-3Cr-3Sn-3Al alloy*, J. Alloys Compd. 803 (2019) 901-911; <https://doi.org/10.1016/j.jallcom.2019.06.323>
- [49] J. Shen, Y. Sun, Y. Ning, H. Yu, Z. Yao, L. Hu, *Superplasticity induced by the competitive DRX between BCC beta and HCP alpha in Ti-4Al-3V-2Mo-2Fe alloy*, Mater. Character. 153 (2019) 304-317; <https://doi.org/10.1016/j.matchar.2019.05.014>
- [50] Y. Namkwon, H.J. Koh, S. Lee, N.J. Kim, Y.W. Chang, *Effects of microstructural evolution on superplastic deformation characteristics of a rapidly solidified Al-Li alloy*, Metall. Mater. Trans. A 32 (2001) 1649-1658; <https://doi.org/10.1007/s11661-001-0143-5>
- [51] W. Zhang, H. Liu, H. Ding, H. Fujii, *The optimal temperature for enhanced low-temperature superplasticity in fine-grained Ti-15V-3Cr-3Sn-3Al alloy fabricated by friction stir processing*, J. Alloys Compd. 832 (2020) 154917; <https://doi.org/10.1016/j.jallcom.2020.154917>
- [52] J. Straska, J. Strasky, P. Minarik, M. Janecek, B. Hadzima, *Continuous measurement of m-parameter for analyzing plastic instability in a superplastic ultra-fine grained magnesium alloy*, Mater. Sci. Eng. A 684 (2017) 10-114; <https://doi.org/10.1016/j.msea.2016.12.027>
- [53] K. Sekiguchi, H. Masuda, H. Tobe, E. Sato, *Continuous recrystallization in dual-phase titanium alloy in superplasticity*, Def. Diff. Forum 385 (2018) 126-130; <https://doi.org/10.4028/www.scientific.net/DDF.385.126>
- [54] A.V. Mikhaylovskaya, O.A. Yakovtseva, I.S. Golovin, A.V. Pozdnyakov, V.K. Portnoy, *Superplastic deformation mechanisms in fine-grained Al-Mg based alloys*, Mater. Sci. Eng. A627 (2015) 31-41; <https://doi.org/10.1016/j.msea.2014.12.099>
- [55] T. Kanazawa, H. Masuda, H. Tobe, K. Kakehi, E. Sato, *Initial process of continuous dynamic recrystallization in a superplastic Al-Mg-Mn alloy*, J. Jap. Inst. Light Met. 67 (2017) 95-100; <https://doi.org/10.2464/jilm.67.95>
- [56] H. Watanabe, K. Kurimoto, T. Uesugi, Y. Takigawa, K. Higashi, *Isotropic superplastic flow in textured magnesium alloy*, Mater. Sci. Eng. A558 (2012) 656-662; <https://doi.org/10.1016/j.msea.2012.08.070>
- [57] M. Myshlyaev, S. Mironov, G. Korznikova, T. Konkova, E. Korznikova, A. Aletdinov, G. Khalikova, *EBSDB study of superplastically strained Al-Mg-Li alloy*, Mater. Letter 275 (2020) 128063; <https://doi.org/10.1016/j.matlet.2020.128063>
- [58] H. Masuda, E. Sato, *Diffusional and dislocation accommodation mechanisms in superplastic materials*, Acta Mater. 197 (2020) 235-252; <https://doi.org/10.1016/j.actamat.2020.07.042>
- [59] R.H. Johnson, C.M. Packer, L. Anderson, O.D. Sherby, *Microstructure of superplastic alloys*, Phil. Mag. 156 (1968) 1309-1314

- [60] V.A. Likhachev, M.B. Myshlyaev, O.N. Sen'kov, S.P. Belyayev, *Creep of aluminum in torsion under superplastic conditions*, Phys. Metal. Metallogr. 52 (1981) 156-164
- [61] J.W. Edington, *Microstructural aspects of superplasticity*, Met. Trans. 13A (1982) 703-715
- [62] A.J. Shakesheff, P.G. Partridge, *Superplastic deformation of Al-Li-Cu alloy sheet*, J. Mater. Sci. 21 (1986) 1368-1376
- [63] B.L. Adams, S.I. Wright, K. Kunze, Orientation imaging: The emergence of a new microscopy, Metall. Mater. Trans. 24A (1993) 819-831; <https://doi.org/10.1007/BF02656503>
- [64] M.M. Myshlyaev, S.Y. Mironov, E.V. Konovalova, *TEM and EBSD investigation of the structural state under high-strength superplastic flow in ECAP aluminum alloy*, Crystallogr. Rep. 54 (2009) 1051-1057; <https://doi.org/10.1134/S1063774509060200>
- [65] M.M. Myshlyaev, M.A. Prokunin, and V.V. Shpeizman, *Mechanical behavior of microcrystalline aluminum-lithium alloy under superplasticity conditions*, Phys. Solid State 43 (2001) 865–870; <https://doi.org/10.1134/1.1371367>
- [66] M.M. Myshlyaev, S.Y. Mironov, E.V. Konovalova, M.M. Kamalov, M.A. Prokunin, M.M. Myshlyaeva, *Structural state and superplasticity of an aluminum-lithium alloy subjected to equal-channel-angular pressing*, Phys. Metal. Metallogr. 102 (2006) 328–332; <https://doi.org/10.1134/S0031918X06090146>
- [67] M.M. Myshlyaev, V.V. Speizman, V.V. Klubovich, M.M. Kulak, G. Lyu, *Change in characteristics of superplastic deformation of the aluminum-lithium alloy under the effect of ultrasonic vibrations*, Phys. Sol. State. 57 (2015) 2039-2044; <https://doi.org/10.1134/S1063783415100236>
- [68] T.R. Bieler, R.S. Mishra, A.K. Mukherjee, Superplasticity in hard-to-machine materials, Annu. Rev. Mater. Sci. 26 (1996) 75-106; <https://doi.org/10.1146/annurev.ms.26.080196.000451>
- [69] S. Li, I.J. Beyerlein, M.A.M. Bourke, *Texture formation during equal channel angular extrusion of fcc and bcc materials: comparison with simple shear*, Mater. Sci. Eng. A394 (2005) 66-77; <https://doi.org/10.1016/j.msea.2004.11.032>
- [70] A.A. Mazilkin, M.M. Kamalov, and M.M. Myshlyaev, *Structure and phase composition of an Al-Mg-Li-Zr alloy under high-rate superplasticity conditions*, Phys. Solid State 46 (2004) 1456–1461; <https://doi.org/10.1134/1.1788778>
- [71] J. Savoie, Y. Zhou, J.J. Jonas, S.R. Macewen, *Textures induced by tension and deep drawing in aluminum sheets*, Acta Materialia 44 (1996) 587-605; [https://doi.org/10.1016/1359-6454\(95\)00214-6](https://doi.org/10.1016/1359-6454(95)00214-6)
- [72] K. Sotoudeh, P.S. Bate, *Diffusion creep and superplasticity in aluminium alloys*, Acta Mater. 58 (2010) 1909-1920; <https://doi.org/10.1016/j.actamat.2009.11.034>

EBSD study of superplasticity: new insight into a well-known phenomenon

[72] R.C. Gifkins, Grain-boundary sliding and its accommodation during creep and superplasticity, Metall. Trans. A 7 (1976) 1225-1232; <https://doi.org/10.1007/BF02656607>

Figure Captions

Figure 1. Effect of deformation temperature on tension behavior: (a) Engineering stress-strain curves, (b) true stress-true strain curves, and (c) the evolution of m-value with strain

Figure 2. Typical appearance of a failed tension specimen, which was tested at 370°C

Figure 3. Microstructure evolution in the grip section of a specimen tested at 395°C: (a) EBSD grain-boundary map, (b) grain-size distribution, (c) misorientation-angle distribution, (d) measured 111 and 110 pole figures, and (e) rotated pole figures. LD, TD, ND, SPN, and SD denote the longitudinal direction, transverse direction, normal direction, shear plane normal, and shear direction of the ECAP billet, respectively. In (a), LABs and HAGBs are depicted as red and black lines, respectively. In (d), dotted lines indicate the presumed orientations of the shear plane normal and shear direction. In (e), the positions of the ideal A ($(1-11)[110]$) and C ($\{001\}\langle 110\rangle$) simple-shear orientations are shown

Figure 4. Selected portions of EBSD grain-boundary maps showing the microstructure in the gage section of failed specimens as a function of deformation temperature: (a) 320°C (elongation to failure = 469%), (b) 355°C (elongation to failure = 599%), (c) 370°C (elongation to failure = 894%), and (d) 395°C (elongation to failure = 988%). In all cases, LABs and HAGBs are depicted as red and black lines, respectively. Note: The tensile direction for all EBSD maps is shown in the bottom right corner of (a).

Figure 5. Effect of deformation temperature on (a) Fraction of fine grains, (b) mean grain size, (c) grain-size distribution, (d) grain-shape aspect-ratio distribution, (e) mean grain-shape aspect ratio, (f) mean kernel-average misorientation. In (b), error bars show the standard deviation

Figure 6. Selected portions of EBSD kernel-average-misorientation (KAM) maps reflecting the dislocation structure in the gage section of specimens pulled in tension at (a) 320°C, (b) 355°C, (c) 370°C, or (d) 395°C. The KAM color code is shown in the top right corner of (a). In all cases, LABs and HAGBs are depicted as white and black lines, respectively. Note: The tensile direction for all EBSD maps is shown in the bottom right corner of (a).

Figure 7. Typical results for (a) an inverse-pole figure showing the grain orientation relative to the tension direction, (b) the misorientation-angle distribution, and (c) the misorientation-axis distributions derived from EBSD maps taken from the gage section of failed specimens tested at 370°C

Figure 8. Microstructure partitioning in material tested at 320°C: (a) Entire EBSD grain-boundary map, (b) fine-grain microstructure constituent (grain size ≤ 3 μm), and (c) coarse-grain microstructure constituent (grain size > 3 μm). In all cases, LABs and HAGBs are depicted as red and black lines, respectively. Note: The tensile direction for all EBSD maps is shown in the bottom right corner of (a).

Figure 9. Comparison of microstructure characteristics measured in the fine-grain and coarse-grain areas of material deformed in tension at 320°C: (a) Grain-shape aspect-ratio distribution, (b) misorientation-angle distribution, and (c) kernel-average-misorientation distribution

Figure 10. Inverse pole figures for the tension direction for material deformed at 320°C: (a) Entire data set, (b) fine-grain microstructural constituent, and (c) coarse-grain microstructural constituent.

Figure 11. EBSD texture maps showing the orientation relationship between neighboring grains in material deformed in tension at (a) 320°C, (b) 355°C, (c) 370°C, or (d) 395°C. In the maps, the $\{hk\ell\}<100>$ fiber texture (red color) and $\{hk\ell\}<111>$ fiber texture (blue color) are shown for a 30-degree tolerance. For simplicity, the deviation from the ideal orientation is indicated in the standard stereographic triangle in the top right corner of (a). Note: The tensile direction for all EBSD maps is shown in the bottom right corner of (a).